Journal of Alloys and Compounds 771 (2019) 793–802

Contents lists available at ScienceDirect

Journal of Alloys and Compounds

journal homepage: http://www.elsevier.com/locate/jalcom

# $Fe_2MnGe$: A hexagonal Heusler analogue

S. Keshavarz [a, b], N. Naghibolashrafi [b, c], M.E. Jamer [d], K. Vinson [c], D. Mazumdar [e], C.L. Dennis [f], W. Ratcliff II [d], J.A. Borchers [d], A. Gupta [b, g], P. LeClair [a, b, *]

[a] Department of Physics and Astronomy, University of Alabama, Tuscaloosa, AL 35487, USA
[b] MINT Center, University of Alabama, Tuscaloosa, AL 35487, USA
[c] Tri-campus Materials Science Program, The University of Alabama, Tuscaloosa, AL 35487, USA
[d] NIST Center for Neutron Research, National Institute of Standards and Technology, Gaithersburg, MD 20899, USA
[e] Department of Physics, Southern Illinois University, Carbondale, IL 62901, USA
[f] Material Measurement Laboratory, NIST, Gaithersburg, MD 20899, USA
[g] Department of Chemistry and Department of Chemical and Biological Engineering, University of Alabama, Tuscaloosa, AL 35405, USA

ARTICLE INFO

*Article history:*
Received 20 March 2018
Received in revised form
13 July 2018
Accepted 25 July 2018
Available online 7 August 2018

*Keywords:*
Heusler
Magnetic
Neutron diffraction

ABSTRACT

We synthesized bulk polycrystalline samples of $Fe_2MnGe$ using arc-melting and vacuum annealing. Our experimental investigations revealed that $Fe_2MnGe$ crystallizes in a hexagonal $DO_{19}$ phase at room temperature, in analogy with its "parent" compound $Fe_3Ge$. We find a large saturation magnetization, even larger than that predicted for the tetragonal phase, of approximately 5 $\mu_B$/f.u. at $T = 5$ K, with a Curie temperature of $T_c$~505 K. The large moment and magnetocrystalline anisotropy, along with the possibility of half-metallicity presents $Fe_2MnGe$ as a strong candidate for spin-transfer-torque RAM and other spintronic applications. We do not find evidence for the cubic or tetragonal phases predicted by first-principles theory during these investigations. However, our neutron diffraction investigations were suggestive of a low temperature structural transformation.



## 1. Introduction

Half-metallic Heusler compounds have been the subject of numerous studies for their versatile properties and particularly for their potential applications in spintronics. These ternary intermetallic compounds were introduced by F. Heusler in 1903 with the discovery of strong ferromagnetic properties of $Cu_2MnAl$ [1]. Half-metallicity of these compounds was first suggested by de Groot et al. [2], and Kübler et al. [3] in 1983. At this point, a large number of Heusler compounds have been predicted to be half-metals, and many have been synthesized in bulk, thin film, and powder forms [4,5]. Based on their structure and the number of constituent elements, these compounds are usually categorized into four main groups: full-Heusler ($X_2YZ$), half-Heusler (XYZ), inverse-Heusler ($Y_2XZ$), and quaternary-Heuslers (XX'YZ), where X(X′) and Y are transition metals, and Z is a main group element [6]. All four groups have very similar cubic crystal structures, and the distinctions between them blur considerably if one allows any degree of site disorder or off-stoichiometric compositions (see, for example, the discussion in Ref. [6] on the relationship between full- and inverse-Heusler structures).

Chemical ordering is also known theoretically to be a major factor in preserving the half-metallicity in Heusler compounds [4,7]. Half-metallicity can survive some degree of atomic disorder in cubic Heusler structures [8], and recent studies have shown the presence of half-metallicity in manganese-rich compounds with tetragonal distortion, e.g. $Mn_2YGa$ (Y=Ru, Rh, Pt) [9], $Mn_2YZ$ (Y = Co, Fe, Ni; and Z = Al, Ga, Sn) [10], and $Mn_3Ga$ [11]. Half-metallicity has been also predicted to persist in some of these compounds in a hexagonal $DO_{19}$ ($P6_3/mmc$, space group no. 194 [12,13]) crystal structure [14], which is one of the adopted structures of the "parent" $Fe_3Ge$ compound [15] and the structure assigned to ball-milled $Fe_2MnGe$ by Zhang et al. [16,17]. The half Heusler FeMnGe reported by Buschow et al. [18] also adopts a hexagonal $Ni_2In$ crystal structure from the same space group. Given that the parent $Fe_3Ge$ compound exists in both a cubic low temperature $L1_2$ structure ($Pm\bar{3}m$, space group 221 [12,13]) and a hexagonal high temperature $DO_{19}$ structure, combined with the tendency of Heusler alloys to adopt several different (but very similar) cubic structures, structure determination is of paramount importance. The anticipation of potentially large magnetocrystalline anisotropy in hexagonal $Fe_2MnGe$ would be very attractive for spintronic applications, such as in current perpendicular to plane Giant

* Corresponding author. Department of Physics and Astronomy, University of Alabama, Tuscaloosa, AL 35487, USA.
*E-mail address:* pleclair@ua.edu (P. LeClair).

https://doi.org/10.1016/j.jallcom.2018.07.298

Magnetoresistance (CPP-GMR) and spin-torque-transfer RAM (STT-RAM).

Zhang et al. [16] synthesized $Fe_2MnGe$ by ball milling, and found the $DO_{19}$ structure to be stable above ~500°, with the cubic $DO_3$ structure stable at lower temperatures ($Fm\bar{3}m$, space group 225 [12,13]). A follow-up paper by Zhang et al. [17] found that the $DO_3$ to $DO_{19}$ transformation on heating of as-milled powders was irreversible - once the $DO_{19}$ phase formed, it remained at room temperature even without quenching. Given that ball milling is a non-equilibrium process that can stabilize metastable phases [19,20], our aim is to corroborate that the $DO_{19}$ phase is stable at room temperature and propose site assignments, and to further explore the structure, morphology, and magnetic properties of $Fe_2MnGe$. In particular, we focus first on establishing the microstructure and composition of our arc-melted and annealed samples, particularly to rule out secondary phases or non-uniformities in composition, which were lacking in previous studies.

At odds with the experimental reports [16,17] is a recent theoretical survey [21] via density functional theory (DFT), which suggested that $Fe_2MnGe$ was thermodynamically stable in the tetragonal $DO_{22}$ structure ($I4/mmm$, space group 139 [12,13]), with a ground state saturation magnetization of approximately 3.00 $\mu_B$/f.u. a spin polarization of 97% at the Fermi level, and a lattice parameter of $a \approx 0.569$ nm with $c/a \approx 0.9839$ [21]. The $DO_{22}$ structure can be considered as a tetragonal distortion of the more common $L2_1$ ($Fm\bar{3}m$, space group no. 225 [12,13]) full Heusler structure. To be fair, this study [21] was limited to cubic and tetragonally-distorted structure, and did not consider whether hexagonal $DO_{19}$ $Fe_2MnGe$ might be more stable than the tetragonal $DO_{22}$ form. Nonetheless, $Fe_2MnGe$ may be a suitable candidate for experimental investigations of half-metallic full-Heuslers, if the tetragonal phase could be synthesized.

In order to experimentally investigate the $Fe_2MnGe$ system, polycrystalline samples of $Fe_2MnGe$ were prepared by arc-melting of the constituent elements in an argon atmosphere and remelting several times to ensure thorough mixing. As-cast samples were later heat treated at various annealing temperatures for different soaking periods to improve their crystalline quality. The effect of the cooling rate was tested by both slow oven-cooling and ice-quenching of the samples. Microstructural studies using Scanning Electron Microscopy (SEM) with Energy Dispersive Spectroscopy (EDS) revealed a single phase granular microstructure for three $Fe_2MnGe$ sample heat treated at high temperatures. X-ray diffraction (XRD), Transmission Electron Microscopy (TEM) and Electron Backscatter Diffraction (EBSD) analyses of these samples revealed the crystal structure of these sample to be hexagonal $DO_{19}$. Magnetic characterization of these samples showed high saturation magnetization of $M_s \sim 5$ $\mu_B$/f.u. at $T = 5$ K with an estimated Curie temperature of $T_c$~505 K. Neutron diffraction investigations validated the high temperature onset of magnetic order and confirmed the hexagonal $DO_{19}$ structure near room temperature for the 600 °C heat treated sample. The measurements also identified a possible transition to a cubic or tetragonal phase at low temperatures (~200–250 K). However, we have not found any samples with a single phase cubic structure throughout our experimental investigations; the hexagonal phase seems to be dominant in all the prepared samples, consistent with Zhang et al. [16,17].

## 2. Experimental details

### 2.1. Synthesis and thermal treatments

Polycrystalline ingots of $Fe_2MnGe$ were prepared by repeated arc-melting of the constituent pure elements in a Edmund Buehler Mini MAM-1 [22] compact arc melting system under an ultra-high purity Argon (99.999%) pressure of 0.02 Pa. Prior to the arc-melting, elemental Mn chunks were wrapped in quartz wool, placed in vacuum sealed quartz tubes, and heat treated at $T = 900$ °C for 9 h. This procedure is necessary to remove the surface oxide and to avoid any contaminations and oxidization of the final compound. The constituent elements Fe (99.98%, Alfa Aesar [22]), Mn (99.9%, Alfa Aesar [22]), and Ge (99.9%, Alfa Aesar [22]) were mixed in stoichiometric ratios 2:1:1 prior to melting. The mixture of the elements was melted 7 to 10 times and turned over before each melting cycle in order to obtain a homogenized sample. To avoid Mn and Ge-deficiency in the as-cast samples, an additional 5% elemental Mn and Ge were added to the mixture prior to the arc-melting procedure, because of volatility of Mn during arc-melting and the fine powder form of Ge used. We arrived at the targeted stoichiometry by repeatedly checking the as-cast composition.

The as-cast samples were cut and examined by scanning electron microscopy (SEM) and energy dispersive spectroscopy (EDS) analysis in a JEOL 7000 [22] Field Emission Scanning Electron Microscope (FESEM) for homogeneity and stoichiometry. After the uniformity and expected 2:1:1 ratio of Fe:Mn:Ge stoichiometry of the as-cast samples were confirmed, samples were wrapped in the tantalum strips and placed in vacuum-sealed quartz tubes for thermal treatments. Samples were annealed at a wide temperature range from $T_a = 400$ °C to $T_a = 1100$ °C in steps of $\Delta T = 100$ °C (or sometimes less) for different periods of dwell time. Heat treatments were always performed on the as-cast samples, and at the end of the annealing cycle they were slowly-cooled in the furnace. Occasionally, some of the samples were quenched in an ice-water mixture to test the effect of cooling rate on the sample properties. Annealed samples were mounted in a conductive phenol powder using a hot-mounting technique prior to metallography analysis. For chemical etching of the samples Marble, Kalling no. 2 or Kroll etchants [22] were used depending on the sample reaction to the etchant [23].

### 2.2. Characterization

The crystal structure of the samples was investigated in a Bruker D8 Discover X-ray Diffraction [22] system, using a Co K$\alpha$ ($\lambda = 0.179$ nm) source. The uniformity of the crystal structure throughout the samples was studied using electron-back scattered scattering (EBSD) analysis in a JEOL 7000 [22] FESEM. To ensure the absence of precipitates and secondary phases, and to confirm the crystal structure at the microscopic scale, Selected Area Diffraction (SAD) analysis was performed a FEI Tecnai F-20 Transmission Electron Microscope [22]. The magnetic and electrical transport characterizations were studied using Quantum Design Physical Property Measurement System (PPMS) Dynacool [22] with both vibrating sample magnetometry (VSM) and electrical transport features. Neutron diffraction studies were performed on the BT-4 triple axis spectrometer at the NIST Center for Neutron Research.

## 3. Results

### 3.1. Microstructural analysis

Among all the samples prepared, we focus on three heat treatments that yielded single-phase samples: the ones heat treated at $T_a = 600$ °C for 7 days (Sample A), $T_a = 800$ °C for 23 days (Sample B), and $T_a = 900$ °C for 23 days (Sample C). All were slowly-cooled to room temperature in the furnace, and all three treatments showed a uniform granular microstructure, examples of which are shown in Fig. 1. The EDS analysis of these samples revealed the composition of the grains to be $Fe_2MnGe$ within the ~5% instrumental

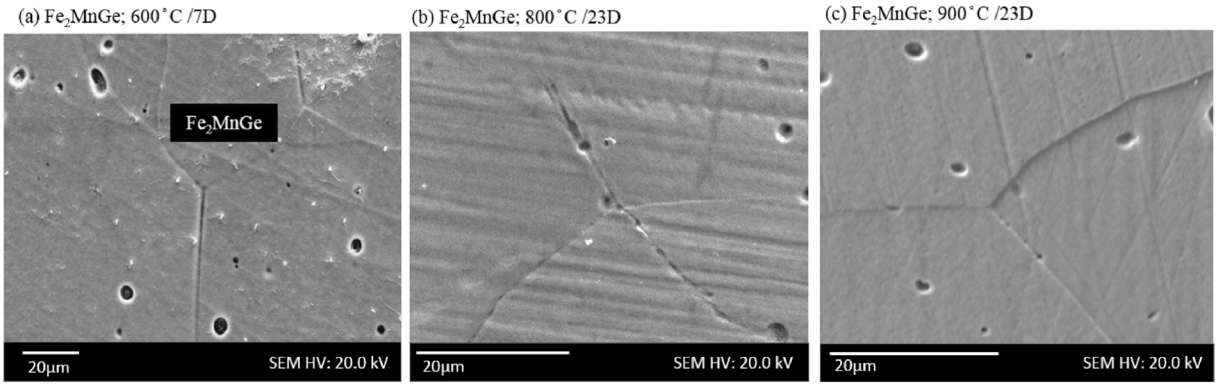


**Fig. 1.** SEM images of the $Fe_2MnGe$ samples showing granular microstructures. Samples were heat treated at (a) $T_a = 600\,^{\circ}C$ for 7 days (Sample A) (b) $T_a = 800\,^{\circ}C$ for 23 days (Sample B), and (c) $T_a = 900\,^{\circ}C$ for 23 days (Sample C) and all slowly cooled to room temperature.

uncertainty range, consistent with the targeted 2:1:1 stoichiometry. No precipitates or secondary phases were observed during these analyses. The crystal structure of these three samples was later confirmed to be the hexagonal $DO_{19}$ structure from both XRD and TEM analyses. All heat treatments in low temperature regimes ($T_a < 600\,^{\circ}C$) resulted in the multiple-phase samples, and purely cubic $L2_1$ or tetragonal $DO_{22}$ phases were never observed during our investigations.

### 3.2. Crystal structure and atomic order analysis

The crystal structures of the annealed $Fe_2MnGe$ samples were investigated by standard X-ray powder diffraction techniques using a Bruker D8 Discover [22] with Co K$\alpha$ radiation ($\lambda = 0.179$ nm). X-ray diffraction patterns for samples B and C are shown in Fig. 2. While we have good reason to believe that $Fe_2MnGe$ will crystallize in the hexagonal $DO_{19}$ structure [16,17], in order to avoid a selection bias we can first determine the crystal class from the XRD data alone, following the procedure in Ref. [24]. From the observed XRD peaks, the values of $\sin^2\theta$ were tabulated. If the structure is in the cubic system, then these values, when properly normalized, will yield a set of integers. Omissions in the list of integers distinguish the type of cubic lattice (sc, bcc, fcc). If there is no overall normalization of the $\sin^2\theta$ values that results in only integral values, the system is not cubic. For the $Fe_2MnGe$ data of Fig. 2, we can deduce that the structure is definitely not cubic. A similar but slightly more involved procedure [24] can be used to test the XRD data against hexagonal systems. We found that the data in Fig. 2 derive from a hexagonal crystal system, and after indexing the peaks, one can deduce lattice parameters of $a \approx 0.522$ nm and $c \approx 0.424$ nm. From our initial list of structures, this leaves only $DO_{19}$ as a possible crystal structure.

As a secondary check, all the postulated crystal structures of $Fe_2MnGe$, including full-Heusler $L2_1$ and its possible disordered phases (e.g. $DO_3$), the hexagonal $DO_{19}$ (space group $P6_3/mmc$, no. 194), the tetragonal $DO_{22}$ (space group $I4/mmm$ no. 139), and the cubic $L1_2$ (space group $Pm\bar{3}m$ no. 221), were simulated using an in-house code, taking into account both the real and imaginary dispersive corrections to the atomic scattering factors [25–27]. Details of the simulated crystal structures, including their prototypes and Wyckoff positions are listed in Table 1. Again, only the hexagonal $DO_{19}$ structure provides a good match to the observed data for the three samples with a purely single-phase microstructure (Samples A, B, and C).

Based on our ($hkl$) indexing of the peaks with the simulated hexagonal crystal structure, and the resulting $d$ spacings

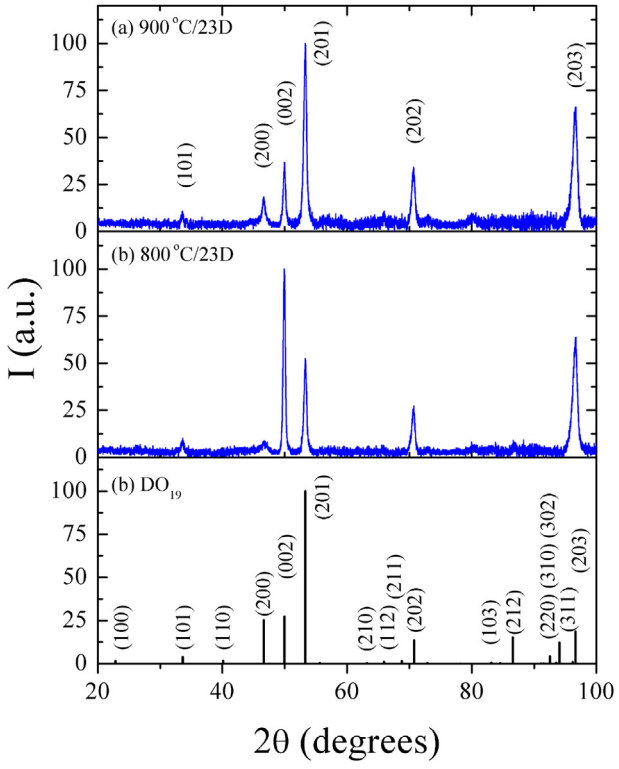


**Fig. 2.** XRD patterns of the $Fe_2MnGe$ samples heat treated at (a) $T_a = 900^{\circ}$ C for 23 days (Sample C), (b) $T_a = 800^{\circ}$ C for 23 days (Sample B), and (c) simulated powder XRD pattern for the $DO_{19}$ $Fe_2MnGe$.

determined by Bragg's law, the lattice parameters $a$ and $c$ can be determined from

$$\frac{1}{d^2} = \frac{4}{3a^2}\left(h^2 + hk + k^2\right) + \frac{l^2}{c^2} \quad (1)$$

Here $d$ is the spacing between the lattice planes, found by Bragg's equation. As with our initial analysis, we found $a \approx 0.522$ nm and $c \approx 0.424$ nm. A more detailed analysis of the diffraction data for sample C using Cohen's method [33] with a Nelson-Riley extrapolation function [34] yields $a = 0.5217 \pm 0.0003$ nm and $c = 0.4237 \pm 0.0003$ nm, which agrees with the results of Zhang et al. [16] within our uncertainty.

A Rietveld refinement was carried out for Samples B and C, using

**Table 1**
Possible crystal structures of $Fe_2MnGe$, with their space group, prototype, and Wyckoff positions.

| Str. | Space Group | Prototype | Wyckoff Positions | Ref. |
|---|---|---|---|---|
| $L2_1$ | $Fm\bar{3}m$ | $Cu_2MnAl$ | Cu @ 8c $(\frac{1}{4},\frac{1}{4},\frac{1}{4})$; Mn @ 4a (0,0,0); Al @ 4b $(\frac{1}{2},\frac{1}{2},\frac{1}{2})$ | [28] |
| $DO_{19}$ | $P6_3/mmc$ | $Ti_3Al$ | Ti @ 6h $(\frac{1}{6},\frac{1}{3},\frac{1}{4})$; Al @ 2d $(\frac{1}{3},\frac{2}{3},\frac{3}{4})$ | [29] |
| $DO_{22}$ | $I4/mmm$ | $Al_3Ti$ | Ti @ 2a (0,0,0); Al @ 2b $(0,0,\frac{1}{2})$; Al@ 4d $(0,\frac{1}{2},\frac{1}{4})$ | [30] |
| $L1_2$ | $Pm\bar{3}m$ | $AuCu_3$ | Au @ 1a (0,0,0); Cu @ 3c $(0,\frac{1}{2},\frac{1}{2})$ | [31] |
| $DO_3$ | $Fm\bar{3}m$ | $BiF_3$ | Bi @ 4a (0,0,0); F @ 4b $(\frac{1}{2},\frac{1}{2},\frac{1}{2})$; F @ 8c $(\frac{1}{4},\frac{1}{4},\frac{1}{4})$ | [32] |

the Crystal Impact Match! [22] and the FullProf programs [35] (Fig. 4). For the final converged fit to the experimental XRD data for Sample B, we found a reduced-$\chi^2 \approx 6.6$, and a reduced-$\chi^2 \approx 5.1$ for Sample C. These values for the goodness of fit parameters are indicative of a highly reliable fit of the simulated $DO_{19}$ pattern to the experimental XRD data. The refined atomic positions have Fe and Mn sharing the 6h sites with 2/3 and 1/3 occupancy, respectively (with the parameter [12,13] $x = 1/6$), and Ge on the 2c sites (Table 2). This structure is shown in Fig. 3. With these site assignments, we simulated the X-ray diffraction pattern with our in-house code. The results are provided in Table 3, where we list the scattering angle $2\theta$ for Co-K$\alpha$ radiation, the reflection indices hkil, relative intensity, and $d$ spacing. For convenience, for the remainder of the manuscript we use the reflection indices hkl.

Finally, even though the identification of the structure as $DO_{19}$ seems fairly certain, we can also investigate the relative XRD peak intensities to clarify the site arrangement. Both through software simulations [25] and by direct calculation of the structure factors, we investigated the consequences of various site assignments. Due to potential texturing in these polycrystalline samples one must exercise caution in interpreting the intensities in too much detail, and we will only consider the gross features of the XRD patterns. Putting the Ge on the 2a or 2b sites results in the (110) peak having the largest overall intensity, but experimentally it is below the noise level of our measurement. Putting Ge on the 2d site would result in the (101) peak having the largest intensity, while experimentally it has extremely weak intensity. Similarly, putting Fe and Mn on the 6g sites rather than the 6h sites would lead to the (100) peak having the highest intensity; experimentally, it is below the noise level.

One might also consider sites 2a, 2d, 2b, 2c for Mn, Fe, Fe, Ge to make a more ordered structure. From our simulations, these assignments make the (110) peak the largest, while the experimental data has this peak below the noise floor. Experimentally the (201) peak is the largest and the (002) peak is roughly 25% as large, while the ordered assignments result in both of them having negligible intensity (~5% of the simulated (110) peak). The same holds for other permutations occupying the 2a-d sites. While texturing and a lack of Fe/Mn X-ray contrast prevents us from doing very detailed quantitative analysis of the peak intensities, even the rough features of the diffraction patterns are not consistent with Fe and Mn

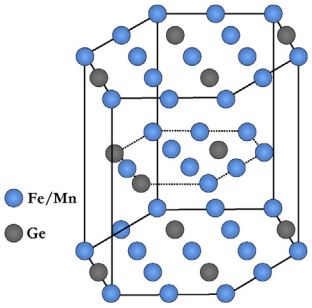


**Fig. 3.** Crystal structure of $DO_{19}$ $Fe_2MnGe$ with $a \approx 0.522$ nm and $c \approx 0.424$ nm. Fe and Mn occupy the sites labeled "Fe".

on any of the 2a-d sites. Only with Fe and Mn on the 6h sites do we have even rough agreement with the diffraction intensities.

Between our simulations and the Rietveld refinement, we conclude that Fe and Mn occupy 6h sites, and Ge the 2c sites in the $DO_{19}$ structure, summarized in Table 2. We note that this is precisely in agreement with the parent $Fe_3Ge$, which has Fe on the 6h sites and Ge on the 2d sites [15]. Thus, $Fe_2MnGe$ can rightly be viewed as a Mn-substituted $Fe_3Ge$ compound. Unfortunately, even aside from the issue of texturing, given the relatively small differences in atomic scattering factors for Fe, Mn, and Ge for Co-K$\alpha$ radiation, it is difficult to draw conclusions about ordering of the sub-lattices, or which 6h sites are Fe and which are Mn (or if indeed there is any ordering), based solely on our XRD measurements. Lacking evidence to the contrary, we assume that Fe and Mn randomly occupy the 6h sites with 2/3 and 1/3 occupancy, respectively. We note that difference in the texture is likely another underlying reason for the difference in relative intensities for Sample B and Sample C.

After all the heat treatments performed on $Fe_2MnGe$ samples, we did not find any sample with uniform cubic Heusler ($L2_1$) phase, nor did we find a transition to a cubic $L1_2$ phase as observed in the parent $Fe_3Ge$ compound [15]. Low temperature heat treatments at $T_a = 400\,^{\circ}C$ and $T_a = 500\,^{\circ}C$ for 7 days and longer resulted in the samples with multiple-phase microstructures, based on both SEM and XRD analyses. Longer heat treatments of 20 days at $T_a = 400\,^{\circ}C$ similarly yielded no cubic phase. A disordered full-Heusler phase

**Table 2**
Proposed Site Assignments for $DO_{19}$ $Fe_2MnGe$.

| | Wyckoff Position | Coordinates | Occ. |
|---|---|---|---|
| Fe | 6h, $x = \frac{1}{6}$ | $(x,2x,\frac{1}{4})\,(-2x,-x,\frac{1}{4})\,(x,-x,\frac{1}{4})\,(-x,-2x,\frac{3}{4})\,(2x,x,\frac{3}{4})\,(-x,x,\frac{3}{4})$ | $\frac{2}{3}$ |
| Mn | 6h, $x = \frac{1}{6}$ | $(x,2x,\frac{1}{4})\,(-2x,-x,\frac{1}{4})\,(x,-x,\frac{1}{4})\,(-x,-2x,\frac{3}{4})\,(2x,x,\frac{3}{4})\,(-x,x,\frac{3}{4})$ | $\frac{1}{3}$ |
| Ge | 2c | $(\frac{1}{3},\frac{2}{3},\frac{1}{4})\,(\frac{2}{3},\frac{1}{3},\frac{3}{4})$ | 1 |

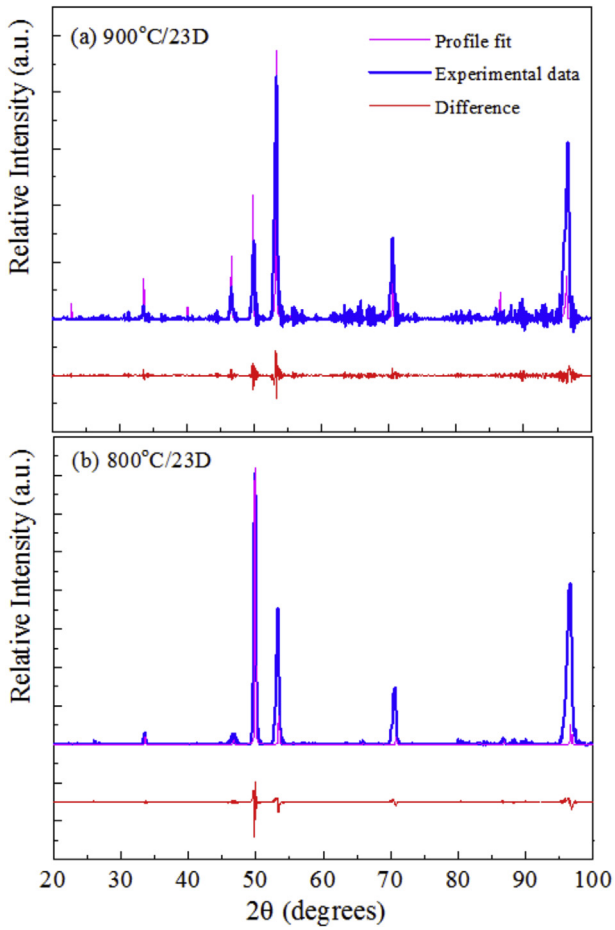


**Fig. 4.** Rietveld refinement of XRD patterns for $Fe_2MnGe$ samples, which were heat treated at (a) $T_a = 900\,^{\circ}C$ for 23 days (Sample C) and (b) $T_a = 800\,^{\circ}C$ for 23 days (Sample B), and both slowly cooled to room temperature.

($DO_3$) was previously reported for powder samples prepared by the planetary ball milling method. According to Ref. [19] and [20], non-equilibrium techniques, such as ball milling and melt-spinning, can retain the meta-stable phases at room temperature. It is possible that cubic and/or tetragonal $Fe_2MnGe$ phases may be metastable, and hence we would not observe them in our samples prepared by arc-melting and annealing, which will reveal only equilibrium phases. Further studies, for example Differential Scanning Calorimetry (DSC) and Differential Thermal Analysis (DTA), might be helpful to investigate the possibility of a phase transition to the cubic phase in the bulk form, but are beyond the scope of this work. Nonetheless, the synthesis of purely hexagonal $Fe_2MnGe$ suggests the possibility of hexagonal Heusler-like compounds in related systems.

As a final check of the sample structure, EBSD analysis was performed, and Fig. 5 shows the EBSD result for Sample C ($T_a = 900\,^{\circ}C$ for 23 days), where the red colored map of the sample is indicative of the uniformity of the hexagonal $DO_{19}$ phase with lattice parameters $a \approx 0.522$ nm and $c \approx 0.424$ nm. An eight hour EBSD scan of this sample with the step size of ~0.5 $\mu$m resulted in approximately 87% $DO_{19}$ phase identification. The zero solution regions (approximately 13%) of the scan seem to be from the sudden changes in the roughness of the sample, which can happen at grain boundaries or from artifacts caused by the metallography and chemical etching procedures, as shown in Fig. 5.

To ensure the uniform crystal structure of the grains at the microstructure level and to test the sample for the presence of any precipitates or secondary phases, the samples were prepared for the Selected Area Diffraction Transmission Electron Microscope (SAED TEM) analysis. As shown in Fig. 6(a), (b), the TEM specimen included three grains of Sample C ($T_a = 900\,^{\circ}C$ for 23 days) to test the consistency of the crystal structure in different grains. The sample was thinned down to <100 nm for sufficient electron transparency and mounted on an omniprobe grid for TEM analysis. SAED TEM analysis was performed in a FEI Tecnai F-20 TEM [22] using a 970 mm camera length. As shown in Fig. 6(c) and (d), the single crystal diffraction patterns from Grain 1 and Grain 2 of this sample were consistent with the hexagonal $DO_{19}$ crystal structure, with lattice parameters $a = 0.522$ nm and $c = 0.424$ nm. From the TEM analysis, the sample seems to be purely single phase, and no diffraction reflections related to secondary phases or precipitates were observed. The satellite reflections around the main diffraction spots are due to the superlattice formation and the long range ordering in the crystal structure of the material [36]. We conclude that the sample is a single phase material with composition $Fe_2MnGe$ and a $DO_{19}$ crystal structure, in agreement with the XRD and EBSD analysis.

**Table 3**
Calculated X-ray diffraction peaks for Co-K$\alpha$ radiation.

| $2\theta$ (°) | hkil | I (a.u.) | $d$ (Å) |
|---|---|---|---|
| 22.84 | $10\bar{1}0$ | 1.56 | 4.521 |
| 33.64 | $10\bar{1}1$ | 3.94 | 3.093 |
| 40.11 | $11\bar{2}0$ | 1.74 | 2.610 |
| 46.65 | $20\bar{2}0$ | 25.2 | 2.260 |
| 49.94 | 0002 | 27.3 | 2.120 |
| 53.32 | $20\bar{2}1$ | 100 | 1.995 |
| 55.59 | $10\bar{1}2$ | 0.401 | 1.919 |
| 63.18 | $21\bar{3}0$ | 0.298 | 1.709 |
| 65.90 | $11\bar{2}2$ | 1.09 | 1.646 |
| 68.77 | $21\bar{3}1$ | 1.48 | 1.585 |
| 70.73 | $20\bar{2}2$ | 13.5 | 1.546 |
| 72.87 | $30\bar{3}0$ | 0.438 | 1.507 |
| 83.13 | $10\bar{1}3$ | 0.518 | 1.349 |
| 84.56 | $21\bar{3}2$ | 0.336 | 1.330 |
| 86.60 | $22\bar{4}0$ | 15.2 | 1.305 |
| 91.09 | $31\bar{4}0$ | 0.153 | 1.254 |
| 93.55 | $30\bar{3}2$ | 0.595 | 1.228 |
| 96.21 | $31\bar{4}1$ | 0.871 | 1.202 |
| 96.64 | $20\bar{2}3$ | 18.6 | 1.198 |
| 104.73 | $40\bar{4}0$ | 2.95 | 1.130 |
| 107.29 | $22\bar{4}2$ | 23.7 | 1.111 |
| 110.08 | $40\bar{4}1$ | 18.1 | 1.092 |
| 110.53 | $21\bar{3}3$ | 0.825 | 1.089 |
| 112.06 | $31\bar{4}2$ | 0.275 | 1.079 |
| 115.20 | 0004 | 4.27 | 1.060 |
| 119.30 | $23\bar{5}0$ | 0.046 | 1.037 |

### 3.3. Magnetic characterization

Magnetic properties of all the heat treated $Fe_2MnGe$ samples were measured using Quantum Design Dynacool [22] at cryogenic and room temperature. As explained earlier, based on our initial DFT calculations and the Slater-Pauling rule, half-metallic full-Heusler ($DO_{22}$) $Fe_2MnGe$ was expected to have a saturation magnetization of approximately 3$\mu_B$/f.u. in its ground state. However, the $DO_{22}$ phase was never observed for this compound throughout our investigations. We performed magnetic characterization on three single-phase $DO_{19}$ samples, Samples A, B, and C described above.

Field-dependent magnetization $M(H)$ curves for Samples A, B,

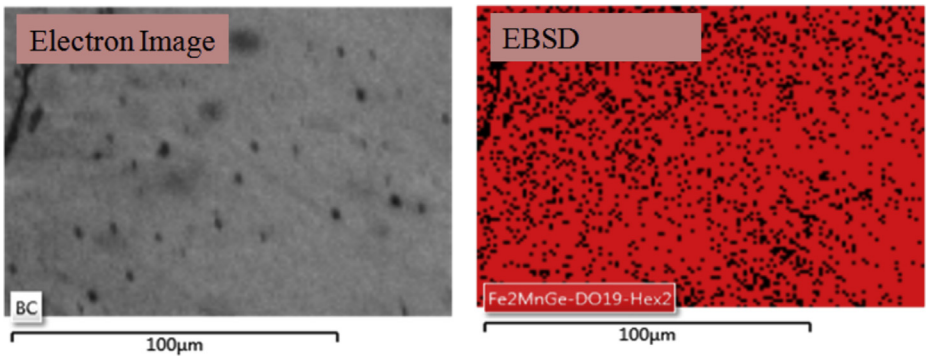


**Fig. 5.** EBSD analysis of the sample confirmed the $DO_{19}$ crystal structure and $Fe_2MnGe$ composition is uniform although the sample (right).

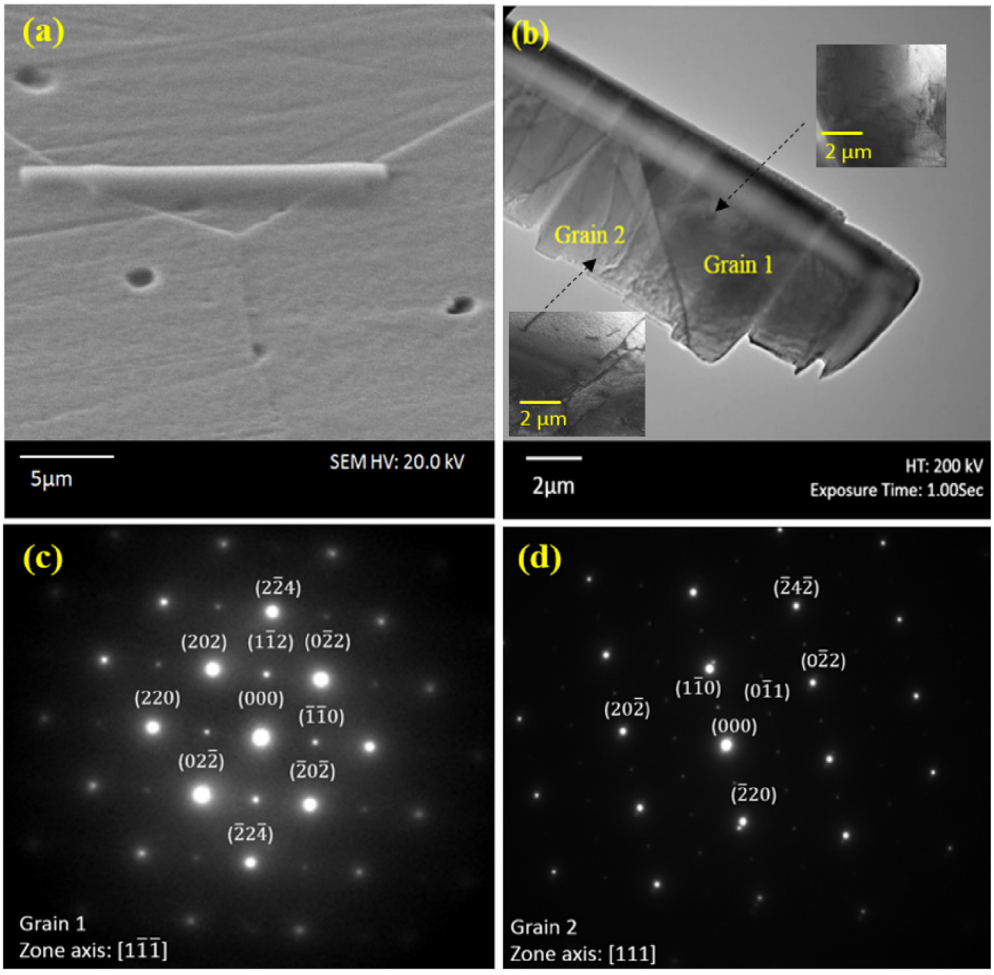


**Fig. 6.** (a) TEM specimen of $Fe_2MnGe$ heat treated at $T_a = 900\,^{\circ}C$ for 23 days (sample C) which consists of three grains (b) TEM specimen prepared by FIB, and (c) Selected area diffraction TEM of Grain 1 for zone axis [1$\bar{1}\bar{1}$], and (d) of Grain 2 for zone axis [111]. The diffraction patterns are consistent with the hexagonal $DO_{19}$ and is indexed with the corresponding crystal structure. The insets of (b) show the bright field images taken from Grain 1 and Grain 2. The dark features on the bright field images represent dislocations. The sample is single phase, no secondary phases were observed in the SAED patterns or the bright field images of both grains.

and C are presented in Fig. 7(a) at low temperature ($T = 5$ K) and room temperature. Compared to the as-cast $Fe_2MnGe$ sample with a saturation magnetization of M ≈ $s$117 $Am^2/kg$ (≈4.24 $\mu_B$/f.u.) at $T = 5$ K, the annealed samples (with a hexagonal structure) have a saturation magnetization of M ≈ $s$113.2 $Am^2/kg$ (≈4.85 $\mu_B$/f.u.) for Sample B and C (heat treated at $T_a = 800\,^{\circ}C$ and $T_a = 900\,^{\circ}C$ for 23 days) and M ≈ $s$117.4 $Am^2/kg$ (≈5.02 $\mu_B$/f.u.) for Sample A (heat treated at $T_a = 600\,^{\circ}C$ for 7 days). The summary of the lattice parameters and the saturation magnetization of the $Fe_2MnGe$ samples with the hexagonal $DO_{19}$ crystal structure are listed in Table 4.

The saturation magnetization of the samples annealed at lower temperatures, $T_a = 400\,^{\circ}C$ and $T_a = 500\,^{\circ}C$ for 7 days, were both approximately M ≈ $s$106.4 $Am^2/kg$ (≈4.56 $\mu_B$/f.u.) at $T = 5$ K. We note again, however, that these samples exhibited *multiple phases*, unlike the single phase samples A, B, and C treated at higher

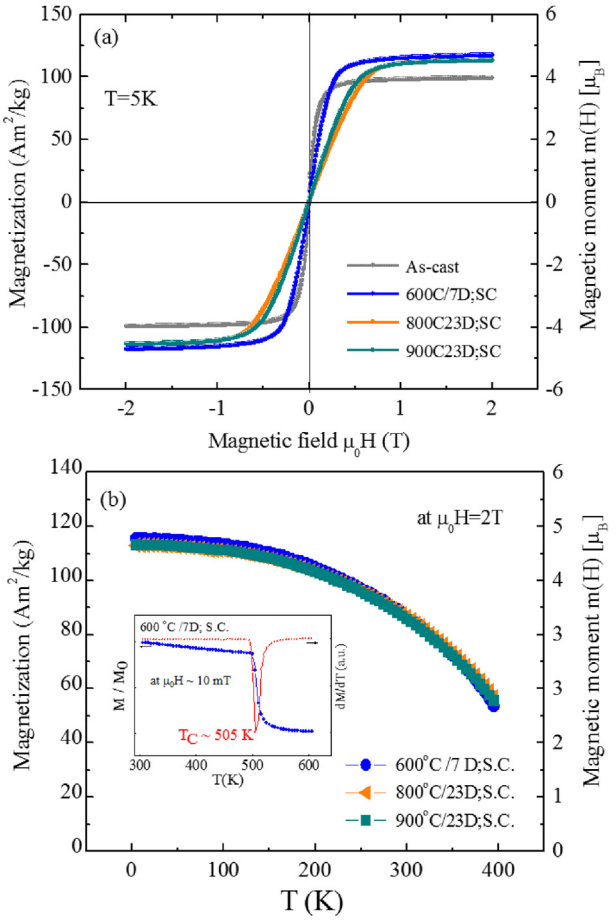


**Fig. 7.** Field-dependent magnetization of as-cast and annealed $Fe_2MnGe$ samples at high temperature shows the high saturation magnetization of the samples. (b) Temperature dependent magnetization of $Fe_2MnGe$ samples during a heating cycle with $\mu_0 H_{ext} = 2$ T. The inset shows the high temperature M(T) of Sample A at $\mu_0 H_{ext} = 10$ mT.

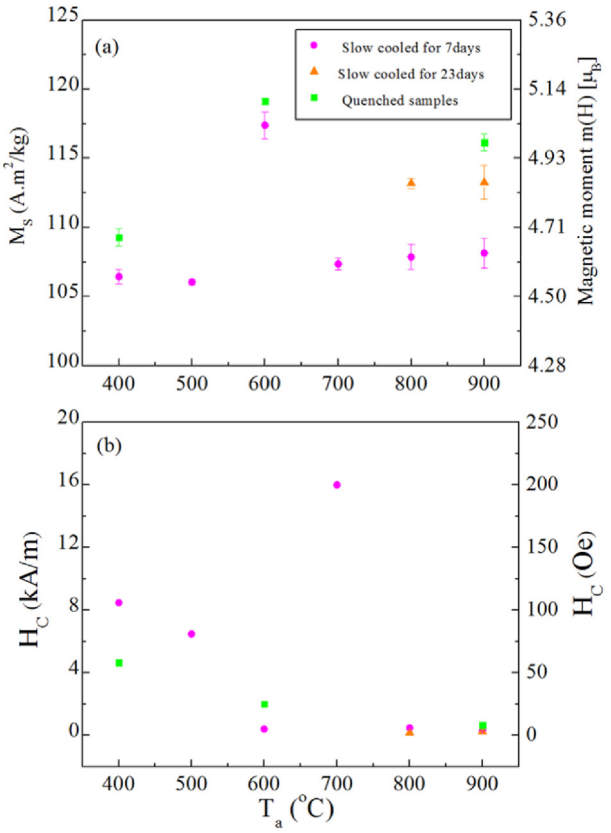


**Fig. 8.** Magnetic properties of $Fe_2MnGe$ as a function of annealing conditions, including (a) the saturation magnetization (at $\mu_0 H_{ext} = 2$ T and $T = 5$ K) and (b) the coercivity.

**Table 4**
Lattice parameters *a* and *c* and the saturation magnetization ($M_s$) of the $Fe_2MnGe$ samples with hexagonal $DO_{19}$ structure.

| Sample | a (nm) | c (nm) | $M_s$ ($\mu_B$/f.u.) | $M_s$ ($Am^2$/kg) |
|---|---|---|---|---|
| A | 0.522(5) | 0.426(7) | 5.02 | 117.3(9) |
| B | 0.522(5) | 0.424(5) | 4.85 | 113.1(9) |
| C | 0.523(1) | 0.424(2) | 4.85 | 113.2(6) |

temperatures. Fig. 8 shows the results of magnetic characterizations of the samples as a function of their annealing conditions, including temperature, dwell time, and the cooling methods (slow-cooled or quenched in ice-water mixture). The coercivity and remanent magnetization of *single phase* samples A, B, and C are very similar: $H_c \approx 2$ kA/m and $M_r \approx 0.4$ $Am^2$/kg. Their saturation magnetization values are highest among most of the heat treated $Fe_2MnGe$ samples. As shown in Fig. 8, the saturation magnetization of all samples are higher than expected for the $DO_{22}$ structure calculated by DFT ($\approx 3.00$ $\mu_B$/f.u.). Temperature-dependent analysis of the samples were performed at $\mu_0 H_{ext} = 2$ T magnetic field during both heating and cooling cycles, from $T = 5$ K to $T = 400$ K, and vice versa. Fig. 7(b) shows the almost overlapping $M(T)$ curves of Samples A, B, and C. The Curie temperature of these samples was estimated to be $T_C$~450 K from fitting the $M(T)$ data to the mean field model for the temperature-dependent magnetization: $M = M_0(T_C - T)^{1/2}$. As shown in inset of Fig. 7(b), a higher temperature measurement of Sample A at $\mu_0 H_{ext} = 10$ mT shows the Curie temperature to be $\sim$ 505 K.

Determining the magnetic anisotropy in these polycrystalline samples presents some difficulty. As an *estimate*, we have used the singular point detection technique [37], where the peak in $d^2M/dH^2$ vs $H$ identifies the anisotropy field $H_a$. This gives $H_a \approx 6 \times 10^5$ A/m for Sample C, and estimating $K_u$ from $K_u = \mu_0 H_a M_s/2$, we find $K_u \sim 3 \times 10^5$ J/m$^3$ at $T = 5$ K (with $M_s = 9 \times 10^5$ A/m). The experimental unit cell density of $\rho = 7958$ kg/m$^3$ of $Fe_2MnGe$ in $DO_{19}$ is used for converting $M_s$ from $Am^2$/kg to A/m. This value of anisotropy constant is close to that of hcp cobalt [38], confirming the high magnetic anisotropy of the hexagonal $DO_{19}$ $Fe_2MnGe$, as predicted from the crystal structure analysis of the material. One should keep in mind that considering the random orientations of grains in the microstructure of the polycrystalline samples, only an effective magnetocrystalline anisotropy can be found. Further, given the irregular shape of our arc-melted samples, demagnetization corrections have not been applied. A better understanding of the magnetic anisotropy in this system requires employing methods, such as transverse susceptibility, ferromagnetic resonance (FMR), and magnetization torque measurements on the prepared materials in thin film or single crystal forms.

### 3.4. Electrical characterization

Electrical transport characterizations were performed using the four point probe and van der Pauw method on the samples of approximately 5mm × 5mm × 3mm in size. The resistivity was

measured during both heating and cooling cycles from $T = 5$ K to $T = 400$ K. As shown in Fig. 9, the sample shows metallic behavior with the residual resistivity ratio RRR = $\rho(300\,\mathrm{K})/\rho(5\,\mathrm{K})$ of around 2.9 and a residual resistivity $\rho_0 \approx 0.96\ \mu\Omega$m at $T = 5$ K. The resistivity appears to be saturating at higher temperatures, suggesting a parallel contribution of the intrinsic $Fe_2MnGe$ resistivity with a higher resistivity varying weakly with temperature [39]. From Matthiessen's rule, we expect the intrinsic resistivity to follow:

$$\rho(T) = \rho_0 + \rho_{e-ph} + \rho_{e-m} = \rho_0 + \alpha T + \beta T^2 \quad (2)$$

where $\rho_0$ is the residual resistivity, and the electron-phonon and electron-magnon scattering processes follow $T$ and $T^2$ temperature dependencies, respectively. We further include a parallel shunting resistivity $\rho_{shunt}$ due to the grain boundaries, and assume that the resistivity of the presumably highly disordered grain boundaries varies negligibly with temperature, leading to the following expression for the resistivity:

$$\frac{1}{\rho_{tot}(T)} = \frac{1}{\rho_i(T)} + \frac{1}{\rho_{shunt}} \quad (3)$$

Fig. 9 shows the result of a nonlinear least-squares fit to this model, with $\rho_0 \approx (1.27\pm0.01)\ \mu\Omega$m , $\alpha = (4.82\pm0.26) \times 10^{-3}\ \mu\Omega\mathrm{m}/K$, $\beta = (9.46\pm0.19) \times 10^{-5}\ \mu\Omega\mathrm{m}/K^2$, and $\rho_{shunt} = (3.69\pm0.01)\ \mu\Omega$m, with a reduced $\chi^2 = 2 \times 10^{-8}$. Here the ± indicate the uncertainties of the best-fit parameters. With these parameters, the electron-magnon contribution will dominate above approximately 50 K. One can also extract the intrinsic resistivity $\rho_i$ from (Eq. (3)), $\rho_i = \rho_{shunt}\rho_{tot}/(\rho_{shunt} - \rho_{tot})$. The extracted $\rho_i$ versus $T^2$ is shown in the inset to Fig. 9 along with a linear fit, also indicating that electron-magnon scattering is the dominant contribution to the resistivity temperature dependence at higher temperatures.

### 3.5. Neutron diffraction

To examine the temperature dependence of the magnetic and structural order, neutron diffraction measurements were taken at the NIST Center for Neutron Research on the BT-4 triple axis spectrometer using $E = 30.5$ meV ($\lambda = 0.1637$ nm). Sample A (heat treated at $T_a = 600\,^\circ$C for 7 days) was fully characterized as a function of temperature during two heating cycles, first from 50 K to 350 K and then from 50 K to 540 K. Additional measurements were subsequently taken upon cooling from 540 K to 200 K. Consistent with the room temperature x-ray diffraction results, the most prominent peaks evident at 200 K during the first heating cycle (Fig. 10) match those expected for the $DO_{19}$ hexagonal structure. The 200 K pattern sharply contrasts with those obtained at 50 K during both the first and second heating cycle (Fig. 10), in which the intensities of the (002), (202) and (203) hexagonal reflections have significantly lower intensity. Systematic examination of the intensity of (202) hexagonal peak as a function of temperature (with selective scans shown in Fig. 10 [left inset]) indicates that the structural ordering progressively evolves during consecutive heating and cooling cycles. Specifically, while the peak is most intense at 200 K during the first heating cycle, it almost disappears at 50 K during both the first and second cycles. The (202) intensity increases again at 250 K during the second cycle and remains approximately constant upon heating up to 450 K.

Coincident with the apparent suppression of the hexagonal peaks at 50 K, new peaks emerge, for example, near $2\theta = 79.5^\circ$ and $49.7^\circ$ (Fig. 10, marked with asterisk). This could be a sign of a low temperature cubic or tetragonal phase, as is observed in $Fe_3Ge$, or it could simply be a distortion of the $DO_{22}$ structure. Unfortunately, the exact characteristics of this mixed phase cannot be determined since the diffraction pattern changes subtly upon thermal cycling, as demonstrated by differences in the 50 K diffraction patterns shown in Fig. 10. The 50 K data obtained during the second heating cycle, however, can be approximately indexed to a cubic structure with the lattice parameter of $a = 0.578 \pm 0.009$ nm, which is close to the calculated value for $DO_{22}$ $Fe_2MnGe$ [21]. However, due to the lack of peaks in this low temperature secondary structure, we cannot convincingly determine the nature of the secondary peaks observed. It is possible that a new structural phase or distortion could be further stabilized with additional thermal cycling as it seemed to be prevalent in the final 200 K diffraction scan (not shown) obtained after cooling from 540 K.

In addition to these findings, we have also determined that the peak near $2\theta = 30.8^\circ$, which indexes to the hexagonal (101), seems to have a magnetic contribution, consistent with previous investigations of the parent compound $Fe_3Ge$, $(Mn_{1-x}Fe_x)_3Ge$ [40], and similar compound FeMnGe [41]. Hori et al. showed that at $Mn_{2.65}Fe_{0.55}Ge$ $D0_{19}$ (101) displayed a unique magnetic contribution in the antiferromagnetic regime, but did not investigate the ferromagnetic regime. The intensity of this reflection decreased continuously as the temperature was increased to 540 K during the second heating cycle, and it increased upon cooling (Fig. 10 [right inset]). This behavior is suggestive of a ferromagnetic order parameter with a $T_C$ that approximates that obtained from bulk magnetometry (Fig. 7(b)). It is possible, however, that this (101) peak has a structural contribution that varies as the sample undergoes the structural transition near 200 K - 250 K. Only the (101) hexagonal peak exhibited a systematic dependence upon temperature that is consistent with the magnetic ordering, and it is possible that the ferromagnetism detected using magnetometry (Fig. 7(b)) originates only from the structural hexagonal phase at all temperatures.

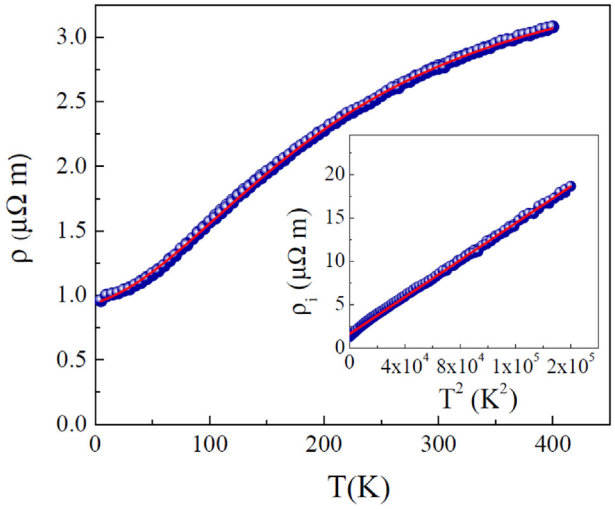


**Fig. 9.** Temperature-dependent resistivity of $Fe_2MnGe$ sample A during the cooling cycle and in the absence of magnetic fields. The solid line is a fit to the model described in the text. The inset shows the intrinsic resistivity, $\rho_i$, as a function of $T^2$. The solid line is a linear fit.

## 4. Discussion

In contrast with recent theoretical predictions for the thermodynamic stability of $Fe_2MnGe$ in the $DO_{22}$ structure, the hexagonal $DO_{19}$ phase was found to be the stable structure of this compound

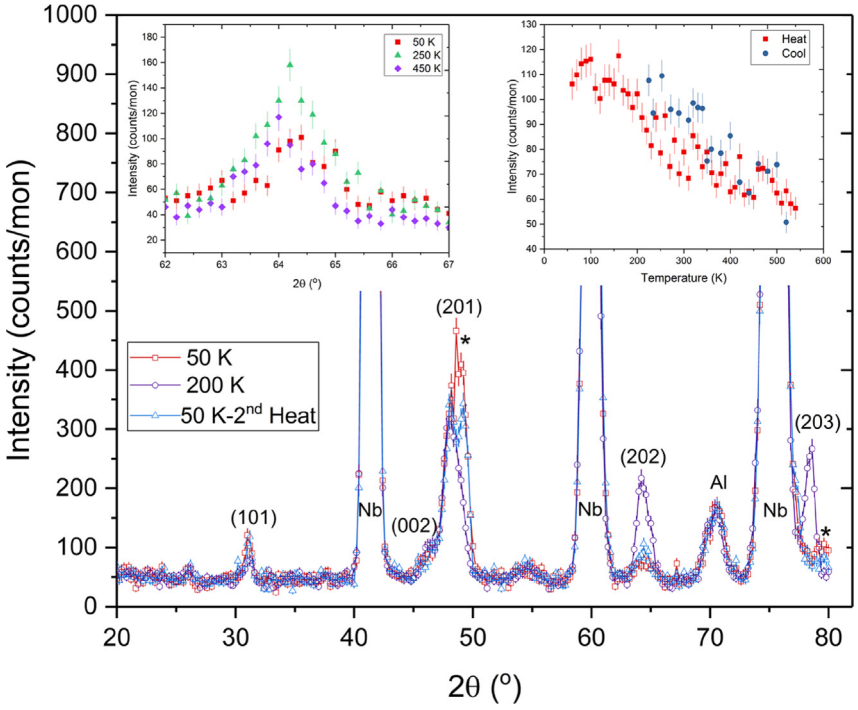


**Fig. 10.** Neutron diffraction of Sample A during first heating cycle at T = 50 K and 200 K and during the second heating cycle at 50 K. The peak indices refer to the $DO_{19}$ hexagonal structure. (inset, left) Neutron diffraction scans through the (202) hexagonal reflection at temperatures of 50 K, 250 K, and 450 K, (inset, right) Temperature-dependent intensity (101) peak during the second heating and the final cooling cycles.

from our experimental investigations, in agreement with Zhang et al. [16,17] The hexagonal structure was observed as the dominant phase at all thermal treatments as measured using room temperature XRD. Throughout our experimental investigations of this system, we never found a single phase tetragonal or cubic structure related to the $DO_{22}$, $DO_3$ or $L2_1$ phases. However, the neutron diffraction results were suggestive of a structural transition at low temperatures. L. Zhang et al. [16,17] have reported the presence of a cubic $DO_3$ (partially disordered full-Heusler phase) at low temperature for the powder form of $Fe_2MnGe$ prepared by planetary ball milling synthesis. Their results based on the Differential Scanning Calorimetry (DSC) and the X-ray diffraction analysis shows that $Fe_2MnGe$ undergoes a phase transition from a cubic $DO_3$ at low temperatures to a hexagonal $DO_{19}$ phase at high temperatures (around a transformation temperature of 527 °C). Similar behavior is observed for $Fe_3Ge$ [42], which goes through a phase transition from a cubic $L1_2$ phase at low temperatures (<700 °C) to a hexagonal $DO_{19}$ phase at higher temperatures (>700 °C). A similar phase transition was also observed for $Mn_{3.4}Ge$ from a low temperature (<680 °C) tetragonal $DO_{22}$ phase to a high temperature (>680 °C) hexagonal $DO_{19}$ phase [43]. Despite the previously observed phase transformation in powdered $Fe_2MnGe$, no purely cubic or tetragonal phase was observed for our bulk samples. Therefore, the cubic phase might be a metastable phase, as suggested by Ref. [17], which only shows up with techniques such as ball milling or thin film growth where the metastable phases can be stabilized. It is also possible that the substitution of Mn in place of Fe stabilizes the hexagonal $DO_{19}$ phase of the parent $Fe_3Ge$ to much lower temperatures, this would be an interesting theoretical investigation in the future.

The high magnetic moment and potentially high magnetocrystalline anisotropy of the hexagonal phase materials may make $Fe_2MnGe$ useful for spintronic applications such as STT-RAM and CPP-GMR. Half-metallicity can survive some degree of atomic disorder and tetragonal distortion for the Mn-rich Heusler-like compounds, and it is expected to persist in hexagonal crystal structures. Further DFT calculations for the hexagonal $DO_{19}$ phase are necessary to confirm whether $Fe_2MnGe$ can be expected to be half metallic. Hexagonal *half-Heusler* compounds, such as LaCuSn, ScCuSn, and YCuSn were previously suggested by Casper et al. [14]. Their crystal resembles a stuffed wurtzite structure with $Ni_2In$ as the prototype. These compounds have pseudo band gaps around the Fermi energy in one of their spin channels, which is the sign of their half-metallicity. We suggest a similar study for $Fe_2MnGe$ and other full Heusler compositions, with a view to understand the stability of the hexagonal phase over cubic phases that appear to be at least metastable.

## 5. Conclusions

To summarize, polycrystalline bulk form samples of $Fe_2MnGe$ were synthesized by the arc-melting technique and annealed in order to find the half-metallic Heusler phase of this compound. During these investigations, we found the stable phase to be a compound with a hexagonal $DO_{19}$ crystal structure at room temperature and high saturation magnetization of $M \approx s5\ \mu_B$/f.u. was found. Strong ferromagnetic character along with high magnetocrystalline anisotropy are the significant properties of this compound. Further investigations of magnetic anisotropy in epitaxial thin films are a logical next step, as is a determination of transport spin polarization using, e.g., Point Contact Andreev Reflection (PCAR) or spin-polarized tunneling. Additional work with neutron diffraction to determine magnetic ordering and x-ray magnetic circular dichroism to determine element-specific moments are underway. Theoretically, the stability of the hexagonal phase in this and related full Heusler composition compounds is worthy of investigation.

## Acknowledgements

This study was financially supported by NSF DMREF Grant Nos. 1235396 and 1235230, and NSF Grant No. DMR 1508680. This work utilized resources owned and maintained by the Central Analytical Facility, which is supported by The University of Alabama.

## References

[1] F. Heusler, W. Starck, E. Haupt, Über magnetische manganlegierungen, Verhandlungen Dtsch. Phys. Ges. 12 (1903) 219.
[2] R. De Groot, F. Mueller, P. Van Engen, K. Buschow, New class of materials: half-metallic ferromagnets, Phys. Rev. Lett. 50 (25) (1983) 2024.
[3] J. Kübler, A. William, C. Sommers, Formation and coupling of magnetic moments in Heusler alloys, Phys. Rev. B 28 (4) (1983) 1745.
[4] T. Graf, C. Felser, S.S. Parkin, Simple rules for the understanding of Heusler compounds, Prog. Solid State Chem. 39 (1) (2011) 1–50. https://doi.org/10.1016/j.progsolidstchem.2011.02.001.
[5] C. Felser, G.H. Fecher, Spintronics from Materials to Devices, Springer, Netherlands, 2013.
[6] L. Wollmann, S. Chadov, J. Kübler, C. Felser, Magnetism in cubic manganese-rich Heusler compounds, Phys. Rev. B 90 (2014) 214420, https://doi.org/10.1103/PhysRevB.90.214420.
[7] I. Galanakis, K. Özdoğan, B. Aktaş, E. Şaşioğlu, Effect of doping and disorder on the half metallicity of full heusler alloys, Appl. Phys. Lett. 89 (4) (2006), 042502, https://doi.org/10.1063/1.2235913.
[8] Y. Miura, K. Nagao, M. Shirai, Atomic disorder effects on half-metallicity of the full-Heusler alloys $Co_2(Cr_{1-x}Fe_x)Al$: a first-principles study, Phys. Rev. B 69 (2004) 144413, https://doi.org/10.1103/PhysRevB.69.144413.
[9] L. Wollmann, S. Chadov, J. Kübler, C. Felser, Magnetism in tetragonal manganese-rich Heusler compounds, Phys. Rev. B 92 (2015), 064417, https://doi.org/10.1103/PhysRevB.92.064417.
[10] C. Felser, V. Alijani, J. Winterlik, S. Chadov, A.K. Nayak, Tetragonal heusler compounds for spintronics, IEEE Trans. Magn. 49 (2) (2013) 682–685, https://doi.org/10.1109/TMAG.2012.2223661.
[11] S. Mizukami, A. Sakuma, A. Sugihara, T. Kubota, Y. Kondo, H. Tsuchiura, T. Miyazaki, Tetragonal $D0_{22}$ $Mn_{3+x}Ge$ epitaxial films grown on MgO(100) with a large perpendicular magnetic anisotropy, Appl. Phys. Express 6 (12) (2013) 123002.
[12] T. Hahn, A. Looijenga-Vos, M.I. Aroyo, H.D. Flack, K. Momma, P. Konstantinov, The 230 space groups, in: M. Aroyo (Ed.), International Tables for Crystallography Volume A: Space-group Symmetry, Springer Netherlands, Dordrecht, 2016, pp. 193–687, https://doi.org/10.1107/9780955360206000114.
[13] M.J. Mehl, D. Hicks, C. Toher, O. Levy, R.M. Hanson, G.L.W. Hart, S. Curtarolo, The AFLOW library of crystallographic prototypes: Part 1, Comput. Mater. Sci. 136 (2017) S1–S828, https://doi.org/10.1016/j.commatsci.2017.01.017.
[14] F. Casper, C. Felser, R. Seshadri, C.P. Sebastian, R. Pöttgen, Searching for hexagonal analogues of the half-metallic half-heusler XYZ compounds, J. Phys. Appl. Phys. 41 (3) (2008), 035002.
[15] P. Villars, $Fe_3Ge$ crystal structure, Inorganic Solid Phases, Springer Materials (online database). URL http://materials.springer.com/isp/crystallographic/docs/sd_0557113.
[16] L. Zhang, E. Brück, O. Tegus, K. Buschow, F. de Boer, The crystallization of amorphous $Fe_2MnGe$ powder prepared by ball milling, J. Alloys Compd. 352 (1–2) (2003) 99–102.
[17] L. Zhang, E. Brück, O. Tegus, K.J. Buschow, F. de Boer, The crystallographic phases and magnetic properties of $Fe_2MnSi_{1-x}Ge_x$, Phys. B Condens. Matter 328 (3–4) (2003) 295–301.
[18] K. Buschow, P. van Engen, R. Jongebreur, Magneto-optical properties of metallic ferromagnetic materials, J. Magn. Magn. Mater. 38 (1) (1983) 1–22.
[19] Z. Ren, S. Li, H. Luo, Structure and magnetic properties of $Fe_2CoGe$ synthesized by ball-milling, Phys. B Condens. Matter 405 (13) (2010) 2840–2843. https://doi.org/10.1016/j.physb.2010.04.008.
[20] Z.H. Liu, H.N. Hu, G.D. Liu, Y.T. Cui, M. Zhang, J.L. Chen, G.H. Wu, G. Xiao, Electronic structure and ferromagnetism in the martensitic-transformation material $Ni_2FeGa$, Phys. Rev. B 69 (2004) 134415, https://doi.org/10.1103/PhysRevB.69.134415.
[21] W.H. Butler, A. Ghosh, K. Munira, T. Lovorn, J. Romero, C. Lample, L. Wilson, J. Ma, Y. Xie, S. Keshavarz, D. Mildebrath, Heusler Database, 2015. http://heusleralloys.mint.ua.edu.
[22] Any mention of commercial products is for information only; it does not imply recommendation or endorsement by NIST
[23] G.F. van der Voort (Ed.), Metallography and Microstructures, ASM Handbook, ASM International, 2004.
[24] B.D. Cullity, S.R. Stock, Elements of X-ray Diffraction, third ed., Prentice Hall, New Jersey, 2001, pp. 299–306. Ch. 10.
[25] P. LeClair, X-ray Diffraction Calculation Software, 2018. http://pleclair.ua.edu/XRD/.
[26] D.C. Creagh, X-ray dispersion corrections, in: E. Prince (Ed.), International Tables for Crystallography Volume C: Mathematical, Physical and Chemical Tables, Springer Netherlands, Dordrecht, 2006, pp. 241–258, https://doi.org/10.1107/97809553602060000103.
[27] P.J. Brown, A.G. Fox, E.N. Maslen, M.A. O'Keefe, B.T.M. Willis, Intensity of diffracted intensities, in: E. Prince (Ed.), International Tables for Crystallography Volume C: Mathematical, Physical and Chemical Tables, Springer Netherlands, Dordrecht, 2006, pp. 554–595, https://doi.org/10.1107/97809553602060000103.
[28] P. Villars, $Cu_2MnAl$ crystal structure, Inorganic Solid Phases, Springer Materials (online database). URL http://materials.springer.com/isp/crystallographic/docs/sd_0459399.
[29] P. Villars, $Ti_3Al$ crystal structure, Inorganic Solid Phases, Springer Materials (online database). URL http://materials.springer.com/isp/crystallographic/docs/sd_0261837.
[30] P. Villars, $Al_3Ti$ ($TiAl_3$ ht) crystal structure, Inorganic Solid Phases, Springer Materials (online database). URL http://materials.springer.com/isp/crystallographic/docs/sd_1013826.
[31] P. Villars, $Cu_3Au$ crystal structure, Inorganic Solid Phases, Springer Materials (online database). URL https://materials.springer.com/isp/crystallographic/docs/sd_1413675.
[32] P. Villars, $Fe_3Ge$ crystal structure, Inorganic Solid Phases, Springer Materials (online database). URL https://materials.springer.com/isp/crystallographic/docs/sd_1251197.
[33] M.U. Cohen, Precision lattice constants from xray powder photographs, Rev. Sci. Instrum. 6 (3) (1935) 68–74, https://doi.org/10.1063/1.1751937.
[34] J.B. Nelson, D.P. Riley, An experimental investigation of extrapolation methods in the derivation of accurate unit-cell dimensions of crystals, Proc. Phys. Soc. 57 (3) (1945) 160.
[35] J. Rodríguez-Carvajal, Recent advances in magnetic structure determination by neutron powder diffraction, Phys. B Condens. Matter 192 (1) (1993) 55–69. https://doi.org/10.1016/0921-4526(93)90108-I.
[36] H. Zandbergen, W. Groen, A. Smit, G. Van Tendeloo, Structure and properties of $(Bi, Pb)_2Sr_2(Ca, Y)$ $Cu_2O_{8+\delta}$, Phys. C Supercond. 168 (3–4) (1990) 426–449.
[37] F. Bolzoni, R. Cabassi, Review of singular point detection techniques, Physica B 346–347 (2004) 524–527, https://doi.org/10.1016/j.physb.2004.01.140.
[38] R. O'Handley, Modern Magnetic Materials: Principles and Applications, Wiley, New York, 2000.
[39] H. Wiesmann, M. Gurvitch, H. Lutz, A. Ghosh, B. Schwarz, M. Strongin, P. Allen, J. Halley, Simple model for characterizing the electrical resistivity in A-15 superconductors, Phys. Rev. Lett. 38 (14) (1977) 782.
[40] T. Hori, Y. Yamaguchi, Y. Nakagawa, Antiferromagnetic to ferromagnetic transition of hexagonal $(Mn_{1-x}Fe_x)_3Ge$, J. Magn. Magn. Mater. 104–107 (1992) 2045–2046.
[41] A. Szytula, A. Pedziwiatr, Z. Tomkowicz, Crystal and magnetic structure of CoMnGe, CoFeGe, FeMnGe, and NiFeGe, J. Magn. Magn. Mater. 25 (1981) 176–186.
[42] A.F. Cabrera, F.H. Sánchez, Mössbauer study of ball-milled Fe-Ge alloys, Phys. Rev. B 65 (2002), 094202, https://doi.org/10.1103/PhysRevB.65.094202.
[43] E. Zavadskiĭ, A. Urushadze, Magnetic properties of Mn-Ge solid solutions, Sov. Phys. - JETP 33 (1971) 138–141 (Zh. Eksp. Teor. Fiz. 60, 251-258).